J Mater Sci: Mater Electron **(2023) 34:2075**

Estimation of microstructural parameters by Williamson–Hall, Halder–Wagner, and size–strain plot methods and magnetic properties of (Cu/Mn) co-doped ZnO nanoparticles

E. Asikuzun Tokeser[1,*], and O. Ozturk[1]

[1] *Department of Metallurgical and Materials Engineering, Faculty of Engineering and Architecture, Kastamonu University, Kastamonu 37200, Turkey*

Received: 29 May 2023
Accepted: 28 September 2023
Published online: 3 November 2023

© The Author(s), under exclusive licence to Springer Science+Business Media, LLC, part of Springer Nature, 2023

ABSTRACT

In this study, all $Zn_{1-x}Cu_{0.05}Mn_xO$ QUOTE $Zn_{1-x}Cu_{0.05}Mn_xO$ QUOTE polycrystalline nanoparticles were produced with various compositions ($0.01 < x < 0.05$) QUOTE ($0.01 < x < 0.05$) QUOTE by using sol–gel techniques. Zinc acetate dihydrate, manganese(II), and Cu(II) acetates were used as the precursors for the solutions. Methanol and acetylacetone were used as solvents while preparing the homogenous solutions. Halder–Wagner method (H–W), Williamson–Hall (W–H), and size–strain plot (SSP) were utilized in order to examine the crystal size and intrinsic strain by X-ray diffraction peak expansion analysis. In addition, different models were developed for the definition of microstructural and physical values including stress, strain, and energy density, in the W–H method. The average crystal sizes determined using W–H, SSP, and H–W methods were compared. The magnetic properties of Cu/Mn-doped zinc oxide nanoparticles were analyzed at room temperature. The highest saturation magnetization (M_s) value was found in the 5% wt Mn doping of ZnO and M_s increased with increasing the Mn doping due to the magnetic (paramagnetic) nature of manganese. In this study, XRD peak broadening analysis has been carried out by different models and X-ray peak profile analysis were used to estimate the physical parameters; different models are modified such as W–H plot, SSP method, and H–W method. D–S method, W–H plot, H–W plot, and SSP technique results were highly intercorrelated.

1 Introduction

ZnO is an n-type semiconductor with a bandgap of 3.37 eV and a high exciton binding energy of 60 meV [1–3]. It is also chemically and thermally stable. It is also cheaper than other known oxides and is environmentally friendly. Zinc oxide has many areas of use including photocatalysts [4, 5], gas sensors [6], white LEDs [7], optoelectronic devices [8, 9], thermoelectric applications [10], and solar cells [11].

Address correspondence to E-mail: easikuzun@kastamonu.edu.tr

https://doi.org/10.1007/s10854-023-11402-w

The properties of ZnO can be altered by doping with different transition metals. Thus, it can be used in various applications such as dilute magnetic semiconductors (DMS). Adding a transition metal remarkably affects the magnetic properties of ZnO by means of the spin effect of electrons. The effect of transition metal ions on the ZnO lattice was investigated by many researchers [12–14].

There are few studies examining the Cu-doped ZnO nanoparticles. The displacement of Cu with the lattice of ZnO changed the properties of ZnO such as photocatalytic activity and magnetic semiconductivity. Since Cu-doped ZnO exhibits fast optical response, these materials have widespread applications in optoelectronic devices, optical switching and waveguides, ultra-fast optic systems of communication, and optical storage [15–17].

ZnO NPs are synthesized by using various methods such as precipitation [18], sol–gel [19], microwave plasma [20], modified polyol method [21], citrate-assisted hydrothermal [22], and electromagnetic levitational gas condensation method [23]. Moreover, when paramagnetic ZnO is doped with a transition metal such as Cr, Mn, Fe, Ni, and Co [24–31], significant changes occur in the magnetic properties of ZnO. As a result, doped ZnO becomes ferromagnetic at room temperature (RT) and this material is a potential candidate for spintronics.

In the present study, a doped ZnO system was prepared by using Mn at different doping ratios (1–5%wt) with the sol–gel method. Besides the structural and microstructural analyses, the magnetic properties were also investigated. The effects of Mn doping will be presented and discussed. The samples were named as Mn1, Mn2, Mn3, Mn4, and Mn5 since Cu0.05 doping is unchanged.

2 Experimental method

2.1 Chemicals and sample preparation

In this study, zinc acetate dihydrate, manganese(II) and Cu(II) acetates powders (purchased from Sigma), methanol, and monoethylamine (as a stabilizer) solvents were mixed using a heater magnetic stirrer for 10 h for all $Zn_{1-x}Cu_{0.05}Mn_xO$ polycrystalline nanoparticles. ZnO-based dilute magnetic semiconductor powder samples were obtained with this method named sol–gel method. The gelled samples were annealed at 600 °C for 30 min and then the resultant powders were pressed. The samples were named Mn1 (1% wt), Mn2 (2% wt), Mn3 (3% wt), Mn4 (4% wt), and Mn5 (5% wt) in accordance with their contribution rates.

2.2 Instruments

The structural characterization was performed using the Bruker D8 Advance X-ray diffractometer. XRD plots of samples examined by using Cu-Kα radiation were given in the Result/Discussion section. It is also very important to determine the magnetic properties of ZnO-based semiconductor materials. In this study, magnetic measurements of the produced Cu/Mn added powder samples were performed by using the Lake Shore 7407 model Vibrating Sample Magnetometer (VSM).

3 Result and discussion

3.1 Analysis methods of X-ray diffraction

The diffraction pattern has its peaks at 31.82°, 34.45°, 36.30°, 47.50°, 56.64°, 62.93°, 66.50°, 68.00°, and 69.16° corresponding to the planes (100), (002), (101), (102), (110), (103), (200), (201), and (112). The JCPDS card number was 36–1451 and ZnO nanocrystals are hexagonal (Fig. 1). XRD peaks were investigated with Scherrer method (SM), modified Scherrer method (MSM), and Williamson–Hall (W–H) analysis to determine the average crystal size.

Given the XRD results, no second phase of Mn and Cu ions was observed. It can be said considering the diffraction patterns, that the intensity of the diffraction peaks decreased with the increase of Mn doping. Increasing the Mn concentration causes deterioration of the crystal structure of ZnO. The ionic radii of Mn^{+2}, Cu^{+2}, and Zn^{+2} ions were found to be 0.80, 0.71, and 0.74, respectively. Since the ionic radius of Mn^{+2} is larger than Zn^{+2}, an increase in the crystal size of nanoparticles is an expected result. Examining the crystal sizes calculated using the Scherrer method (Table 1), it can be seen that the crystal size increased with increasing Mn doping. In addition, as seen in Fig. 1b, the peaks shifted to smaller angles with the increasing Mn doping. This result indicates an increase in the c-axis (Table 1). The increase in lattice parameters might be related with the unit cell volume expansion. It is due

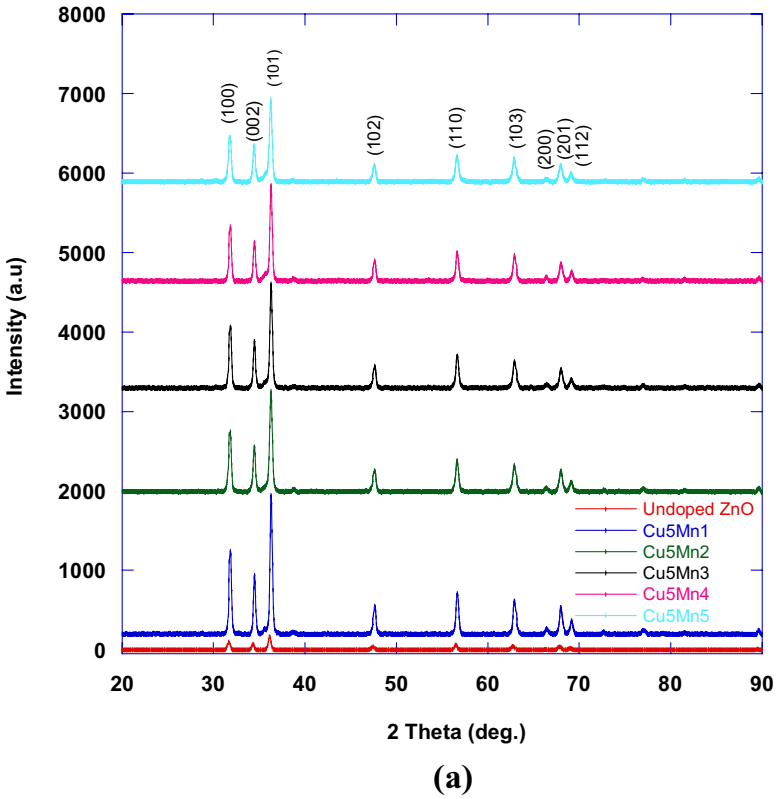

(a)

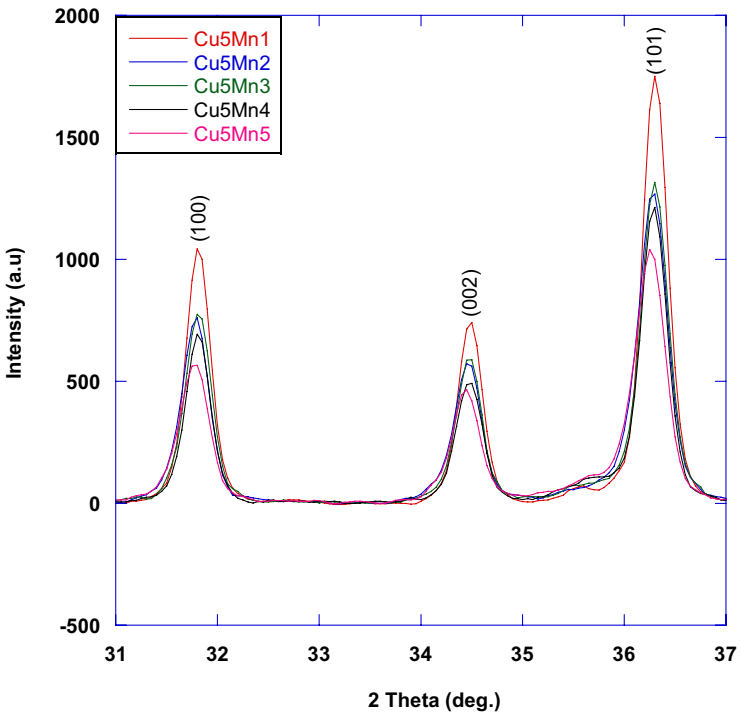

(b)

Fig. 1 XRD peaks for all samples

Table 1 Values of crystal size calculated according to Scherrer and modified Scherrer models

Samples	$a=b$ (Å)	c (Å)	Crystal size Scherrer method (nm)	Crystal size (nm) Modified Scherrer method
Mn1	3.24	5.19	25.06	26.72
Mn2	3.24	5.19	25.65	27.87
Mn3	3.24	5.20	25.29	26.00
Mn4	3.24	5.20	25.41	25.79
Mn5	3.24	5.21	26.09	27.63

to the ionic radius mismatch between the doped Mn^{+2} ion and the host Zn^{+2} ion.

3.1.1 SM

The peak of XRD expands due to the effect of crystal size and intrinsic strain in nanocrystals and this expansion consists of two parts. These are instrumental expansion and physical expansion. The instrumental expansion can be adjusted with Eq. (1).

$$\beta_d^2 = \beta_m^2 - \beta_i^2 \tag{1}$$

β_m and β_i are the measured and instrumental expansions, respectively. The physical and instrumental expansions are determined as full-weight half-maximum. By the adjusted physical expansion, the average crystal size can be determined by using the Scherrer equation.

$$D = \frac{0.9\lambda}{\beta_d}.\frac{1}{\cos\theta} \tag{2}$$

λ and D refer to the radiation wavelength and average crystal size, respectively. This value was found to be 25.06, 25.65, 25.29, 25.41, and 26.09 nm for doped samples, respectively (Table 1).

3.1.2 MSM

The modified Scherrer equation can offer advantages in reducing the number of possible mathematical errors. Equation (3) is obtained by taking the logarithm of all sides of the Eq. (2). When $\ln\beta - \ln(1/\cos\theta)$ QUOTE is plotted, the point where the graph

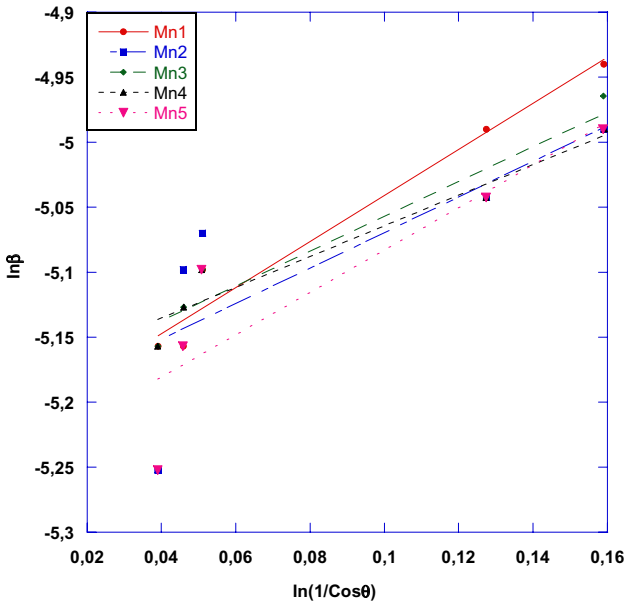

Fig. 2 Modified Scherrer plot for ZnCuMn nanoparticles

intersects the y-axis gives $\ln(k\lambda/D)$. This graph is known as the modified Scherrer graph. Therefore, the average crystal size of ZnCuMn samples can be calculated. The resulting values are summarized in Table 1.

$$\mathrm{In}\beta_d = \mathrm{In}\frac{k.\lambda}{D} + \mathrm{In}\frac{1}{\cos\theta} \tag{3}$$

3.1.3 W–H

The Scherrer method relates only to the XRD peak expansion of the crystal size. But it does not provide information about the internal strain that develops in nanocrystals due to point defects, boundary of grain, stack errors, and triple bonding (Fig. 2). Methods such as W–H and W–A both take into account the strain effect stimulated expansion of the XRD peak and are used in calculating the particle size, as well as internal stress. This analysis is a simplified and quite easy way. Accordingly, the broadening of the physical line of the XRD peak occurs due to the nanocrystal size, the microstrain, and the all expansion can be inscribed as [32]:

$$\beta_{\text{total}} = \beta_{\text{size}} + \beta_{\text{strain}} \tag{4}$$

In this study, average crystal size and microstrain were determined by using the W–H equations developed such as UDM (uniform deformation

model), USDM (uniform stress deformation model), and UDEDM (uniform deformation energy density Model).

3.1.3.1 UDM The UDM takes monotony strain along the crystal direction into account. Deformation occurs in nanocrystals due to defects in the crystal (Fig. 3). This intrinsic strain essentially influences the physical expansion and the peak expansion of the XRD caused by its can be stated as:

$$\beta_{\text{strain}} = 4\varepsilon\tan\theta \tag{5}$$

Thus, the all expansion because of stress and size can be calculated as:

$$\beta_{hkl} = \beta_{\text{size}} + \beta_{\text{strain}} \tag{6}$$

where β_{hkl} refers to the FWHM value.

$$\beta_{hkl} = \frac{k\lambda}{D}\frac{1}{\cos\theta} + 4\varepsilon\tan\theta \tag{7}$$

Rewriting the equation,

$$\beta_{hkl}\cos\theta = \frac{k\lambda}{D} + 4\varepsilon\sin\theta \tag{8}$$

The equation is a linear equation and expressed as the UDM equation that takes the isotropic nature of crystals into account. When the ($\beta_{hkl}\cos\theta$) QUOTE QU−4sinθ graph is plotted, the intrinsic strain and the average crystal size are obtained from the slope and the intercept of the graph, respectively [33].

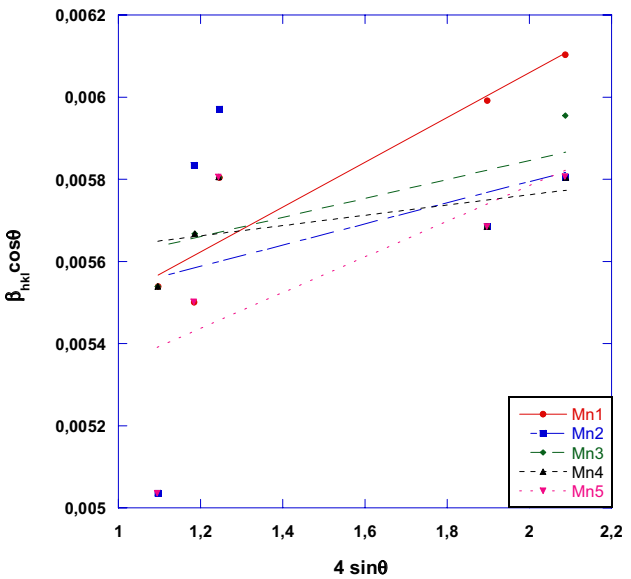

Fig. 3 UDM plot for ZnCuMn nanoparticles

The source of lattice strain is lattice expansion or contraction in nanocrystals due to size reduction. Many defects occur in the lattice structure because of the size limitation and it causes lattice stress.

The slope of the graph obtained was positive, indicating the lattice expansion. In addition, an intrinsic strain was observed in the nanocrystals. The average crystal size obtained by using the uniform deformation model is comparable to the crystal size determined by the Scherrer model (Table 2).

3.1.3.2 USDM According to the UDM model, the sample is isotropic and homogeneous. This is also not true for a crystal. Because a crystal has an anisotropic property, the equation of W–H must be altered with an isotropic term. The model is named as the USDM. Here, the deformation stress of lattice is presumed to be monotony alongside all the lattice plane directions including a small microtension.

With respect to Hooke's law, strain and stress have a linear relationship.

$$\textbf{Stress}: \sigma = \varepsilon Y_{hkl} \tag{9}$$

Here Y_{hkl} is Young's modulus (or elasticity).

$$\textbf{Strain}: \varepsilon = \frac{\sigma}{Y_{hkl}} \tag{10}$$

Due to the size limitation, a small amount of internal stress occurs intrinsic strain in the crystal. USDM considers the broadening of stress induced in the X-ray diffraction peak and the anisotropic (direction dependent) property of the modulus of Young's.

Putting the value of ε in Eq. (8) and on rearranging, we obtain the Eq. (11).

$$\beta_{hkl}\cos\theta = \frac{k\lambda}{D} + 4\sigma\frac{\sin\theta}{Y_{hkl}} \tag{11}$$

It is the W–H-modified equation and is defined as the USDM. The model imagines uniform stress in each crystal direction. Herein, can be stated as follows for the hexagonal crystal.

$$Y_{hkl} = \frac{\left[h^2 + \frac{(h+2k)^2}{3} + \left(\frac{al}{c}\right)^2\right]^2}{S_{11}\left(h^2 + \frac{(h+2k)^2}{3}\right)^2 + S_{33}\cdot\left(\frac{al}{c}\right)^4 + (2S_{13} + S_{44})\cdot\left(h^2 + \frac{(h+2k)^2}{3}\right)\cdot\left(\frac{al}{c}\right)^2} \tag{12}$$

The hexagonal system has five elastic constants.

Table 2 Geometrical parameters of ZnCuMn nanoparticles using different models

Samples	Scherrer method	Williamson-Hall method								
		UDM		USDM			UDEDM			
	Size D (nm)	Size D (nm)	Strain ε (10^{-4})	Size D (nm)	Strain ε (10^{-4})	Stress σ (10^{-2}) (GPa)	Size D (nm)	Strain ε (10^{-4})	Stress σ (10^{-2}) (GPa)	Energy density U (kJ m^{-3})
Mn1	25.06	29.19	5.45	29.19	0.586	0.073	24.79	0.390	0.419	7.29
Mn2	25.65	27.47	2.57	27.48	0.623	0.034	31.55	7.574	8.145	2745.76
Mn3	25.29	26.91	2.31	26.91	0.406	0.030	25.90	0.980	1.019	43.03
Mn4	25.41	26.28	1.25	26.28	0.416	0.016	26.18	1.181	1.269	66.74
Mn5	26.09	26.23	1.13	29.49	0.367	0.058	29.31	4.408	4.775	930.25

Hexagonal matrix

$$\begin{vmatrix} C_{11} & C_{12} & C_{13} & 0 & 0 & 0 \\ C_{12} & C_{11} & C_{13} & 0 & 0 & 0 \\ C_{13} & C_{13} & C_{33} & 0 & 0 & 0 \\ 0 & 0 & 0 & C_{44} & 0 & 0 \\ 0 & 0 & 0 & 0 & C_{44} & 0 \\ 0 & 0 & 0 & 0 & 0 & \frac{1}{2}C_{11} - C_{12} \end{vmatrix}$$

S_{11},S_{13}, S_{33},and $S_{44}$are named as elastic conformities of hexagonal ZnO and are calculated from the values ofC_{11},C_{12},C_{13},C_{33}, and C_{44}given below.

$$S_{11} = \frac{1}{2}\left(\frac{C_{33}}{C_{33}(C_{11}+C_{12}) - 2(C_{13})^2} + \frac{1}{C_{11}-C_{12}}\right) \quad (13)$$

$$S_{12} = \frac{1}{2}\left(\frac{C_{33}}{C_{33}(C_{11}+C_{12}) - 2(C_{13})^2} + \frac{1}{C_{11}-C_{12}}\right) \quad (14)$$

$$S_{33} = \frac{C_{11}+C_{12}}{C_{33}(C_{11}+C_{12}) - 2(C_{13})^2} \quad (15)$$

$$S_{13} = \frac{C_{33}}{C_{33}(C_{11}+C_{12}) - 2(C_{13})^2} \quad (16)$$

$$S_{44} = \frac{1}{C_{44}} \quad (17)$$

The values of hardness constants C_{11}, C_{12}, C_{13}, C_{33}, and C_{44} for hexagonal ZnO are given as 165 GPa, 31.1 GPa, 50 GPa, 61.8 Gpa, and 39.6 GPa, respectively [34, 35].

Using these stiffness constant values, S_{11}, S_{12},S_{33}, S_{13}, andS_{44} elastic compliance values were calculated as 6.28×10^3, -1.18×10^3, 27.54×10^3, -7.02×10^3, and $25.25 \times 10^3 GPa^{-1}$. Using these fitness values, the average Young's modulus value was calculated as 132.44, 132.44, 132.37, 132.37, and 133.73 GPa for (100), (002), (101), (110), and (103) peaks [33].

The $(\frac{4\sin\theta}{Y_{hkl}})/(\beta_{hkl}.\cos\theta)$ graph is given in Fig. 4. The slope of the graph gives the value of the stress, while the intercept gives the average size of the Mn-doped ZnO nanocrystals. Stress and average crystal size values are given in Table 2.

3.1.3.3 UDEDM The UDM model accepts the isotropic creation of the nanocrystal. USDM model claims that there is a linear relationship between stress and strain, as stated in Hooke's law (Fig. 5). How-

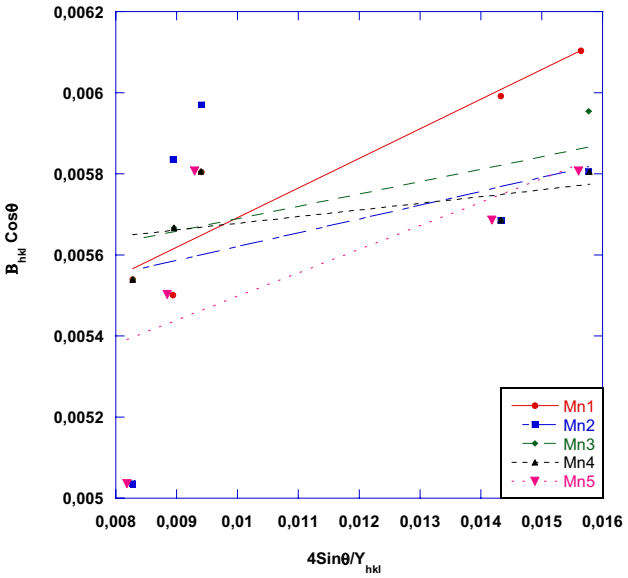

Fig. 4 USDM plot for ZnCuMn nanoparticles

ever, in real crystals, the isotropic form and the linear relationship between stress and strain are ignored due to different dislocations, defects, and clumps in nanocrystals. Therefore, a particular model is needed in order to investigate the particular microstructures of materials.

Here, the UDEDM model considers uniform anisotropic lattice stress in the entire crystal direction. The reason for this stress is the density of the deformation energy.

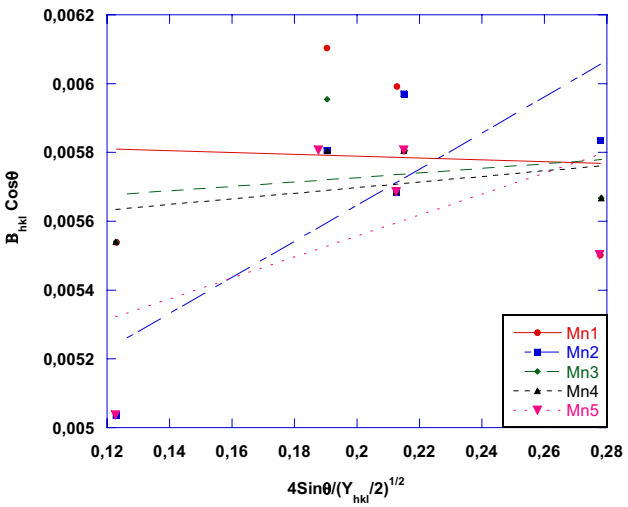

Fig. 5 UDEDM plot for ZnCuMn nanoparticles

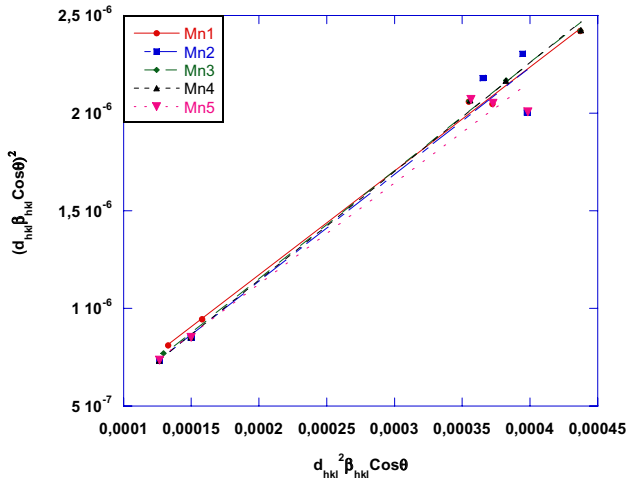

Fig. 6 SSP plot for ZnCuMn nanoparticles

As stated in the Hooke's law, u (energy density) is connected to strain.

$$u = \varepsilon^2 \frac{Y_{hkl}}{2} \tag{18}$$

It is known that strain and stress are related as $\sigma = \varepsilon . Y_{hkl}$. Thus, intrinsic strain can be expressed as a function of u. Putting the value of ε in Eq. (8) and rearranging it, we have the following equation.

$$\beta_{hkl}\cos\theta = \frac{k\lambda}{D} + 4\sin\theta\sqrt{\frac{2.u}{Y_{hkl}}} \tag{19}$$

Equation (19) is a linear equation and it is named as the UDEDM. Using this model, the energy density value can be obtained. The data obtained are given in the Table 2.

(a) SSP (Size–Strain Plot)

The W–H method explains the expansion of the peaks as a function of the 2θ diffraction angle. There are also models that analyze the peak profile. The SSP method explains the lattice strain and crystal size (Fig. 6). This method is more precise, especially at high diffraction angles. The SSP is considered as a combination of the Lorentzian and Gaussian functions (L and G) of the XRD peak profile. The total expansion of the SSP is expressed as follows [36].

$$\beta_{hkl} = \beta_L + \beta_G \tag{20}$$

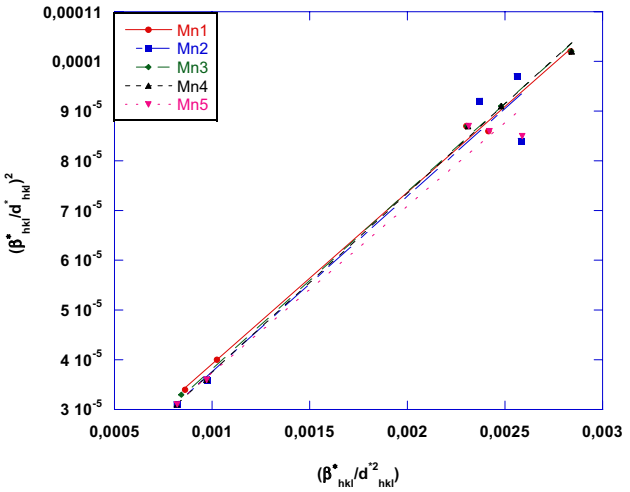

Fig. 7 H-W plot for ZnCuMn nanoparticles

Here, $\beta_L$and β_G refer to the peak expansions arising from the *L* and *G* functions, respectively. Moreover, the size–strain plot gives a preferable result for isotropic expansion.

SSP calculation is performed using the following equation.

$$(d_{hkl}\beta_{hkl}\cos\theta)^2 = \frac{k.\lambda}{D}\left(d_{hkl}^2\beta_{hkl}\cos\theta\right) + \frac{\varepsilon^2}{4} \tag{21}$$

Here, d_{hkl} is called the interplanar distance and given for hexagonal crystal in below:

$$\frac{1}{d_{hkl}^2} = \frac{4}{3}\left[\left(\frac{h^2+k^2+hk}{a^2}\right) + \left(\frac{l}{c}\right)^2\right] \tag{22}$$

Here, d_{hkl}, (hkl) refers to the lattice distance between planes and, for a hexagonal crystal, it is calculated as follows:

$$\frac{1}{d_{hkl}^2} = \frac{4}{3}\left[\left(\frac{h^2+k^2+hk}{a^2}\right) + \left(\frac{l}{c}\right)^2\right] \tag{23}$$

Now, the $\left(d_{hkl}^2.\beta_{hkl}.\cos\theta\right)$–$(d_{hkl}.\beta_{hkl}.\cos\theta)^2$ graph is drawn using Eq. (21). The average particle size is obtained from slope of the graph, whereas the intrinsic strain is obtained from the intercept.

(b) Halder-Wagner (H–W) Method

In the SSP method, the size expansion of the XRD peak is associated with the L and G functions. However, the XRD peak is actually neither an L nor a G function. The H–W method is used in order to explain this situation (Fig. 7). A symmetric Voigt function is used for this method. This function is a transformation of the L and G functions [37]. Thus, for the function of Voigt, the FWHM value of the physical profile can be written by using the H-W method [38–41].

$$\beta_{hkl}^2 = \beta_L\beta_{hkl} + \beta_G^2 \tag{24}$$

Here, β_L and$\beta_G$are the FWHM of the L and G functions, respectively. The advantage of this method is the more weight attached to the peaks in the midangle and low range. The overlap between the diffraction peaks is much less at these angles. Considering the H–W method, the relationship between crystal size and lattice strain is written as follows.

$$\left(\frac{\beta_{hkl}^*}{d_{hkl}^*}\right)^2 = \frac{1}{D}\frac{\beta_{hkl}^*}{d_{hkl}^{*\,2}} + \left(\frac{\varepsilon}{2}\right)^2 \tag{25}$$

$$\beta_{hkl}^* = \beta_{hkl}\cos\theta/\lambda \tag{26}$$

$$d_{hkl}^* = 2\sin\theta/\lambda \tag{27}$$

The $(\beta_{hkl}^*/d_{hkl}^{*\,2})$–$\left(\beta_{hkl}^*/d_{hkl}^*\right)^2$ graph is drawn using Eq. (23). The average crystal size is obtained from slope of the graph, whereas the intrinsic strain of Mn-doped ZnO nanocrystals is obtained from the intercept. The values obtained are summarized in Table 2.

The strain value found from the H–W plot was 10 times higher than the strain values obtained from the other models calculated. The increase in the strain value is essentially due to the addition of medium and low-angle XRD data. Moreover, the higher strain value calculated is associated with the lattice dislocations, which has an important role in the expansion of the reflection peaks at low angles [41].

Given these analyses, it was determined that the average size determined from W–H methods was much closer to the Scherrer method. In our case, the UDM, USDM, and UDEDM models are the most suitable models for the evaluation of the average crystal size of ZnO nanoparticles. As can be seen in Table 2, comparing the crystal sizes calculated using the Scherrer method with XRD data to the crystal sizes calculated with other methods,

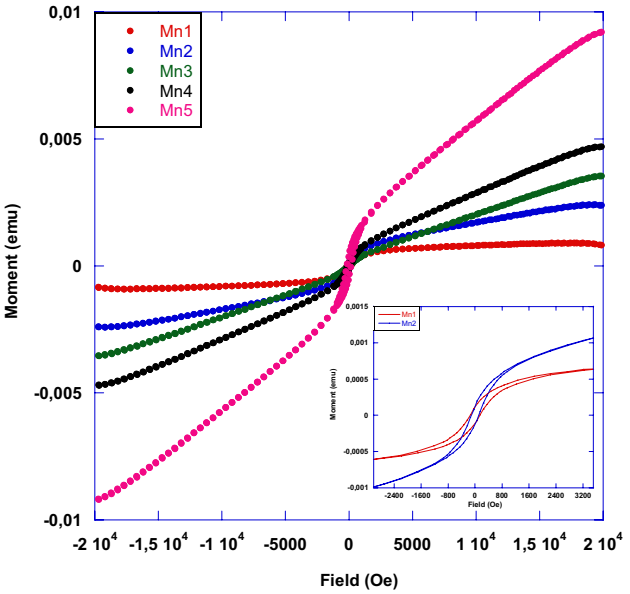

Fig. 8 M-H loop: variation of magnetization with applied field

it can be seen that the UDM method is more successful in determining the crystal size.

3.2 Magnetic analysis results with VSM (vibrating sample magnetometer) measurement

The magnetic properties of Mn/Cu-doped ZnO nanoparticles were measured at RT. The graph of magnetization (M) versus applied magnetic field (H) shows the magnetic properties of all nano-thin films (Fig. 8). The M_s value (saturation magnetization) is the highest for 5% wt Mn doping in ZnO and increased with the increasing Mn doping due to the magnetic (paramagnetic) nature of manganese. Magnetization increases with the accumulation of Mn at the grain boundary. This is also consistent with the existing literature (Table 3).

The saturation and residual magnetization of Cu/Mn-doped ZnO nano-thin films first decreased and then increased with the increase of Mn doping percentage (Fig. 8). The crystal size increased from 25.06 to 26.09 nm. As a result, nanocrystals in the structure form domains, in which all turns are the same with increasing the Mn doping percentage. As the number of moving domains increases, the magnetization will increase in thin films. The lattice parameter increases because Mn^{+2} ions (0.080 nm) have a larger ionic radius than Zn^{+2} ions (0.074 nm). An increase in the lattice parameter increases the saturation magnetization.

Table 3 Some parameters of ZnCuMn nanoparticles

Samples	Size–strain plot		Halder-Wagner method	
	Size D (nm)	Strain ε (10^{-4})	Size D (nm)	Strain ε (10^{-3})
Mn1	27.27	6.62	28.98	4.29
Mn2	26.52	4.37	28.32	3.21
Mn3	26.23	4.39	28.08	3.19
Mn4	26.04	3.59	27.85	2.54
Mn5	28.06	6.07	29.94	3.99

In addition, the increasing saturation magnetization with an increase in Mn doping can be because of the close paramagnetic coupling between Mn^{+2} ions. Different magnetic parameters, H_c (coercivity), exchange bias (E_b), M_r (residual magnetization), M_s, and squareness were calculated using the hysteresis for all thin films and are presented in Table 4. It can be clearly seen that an increase in saturation magnetization results as an increase in H_c. It was reported by many researchers that an increase in M_s and H_c is associated with an increase in crystal size. M_s increases with an increasing crystal size.

Brown's equation relates H_c with the M_s.

$$H_c = H_a = \frac{2K}{\mu_0 M_s} \tag{28}$$

Here, H_a refers to the anisotropy field, K refers to the anisotropy constant, and μ_o refers to the Bohr magneton at zero magnetic fields. The H_c is inversely proportional to the M_s values. Squareness (M_r/M_s) is the ratio between persistence and saturation magnetization. The relationship between the M_r/M_s and M_r is illustrated in Fig. 9 drawn and it can be seen that an increase in M_r caused a decrease in the squareness ratio of the nano-thin films. Figure 10 shows the alteration in exchange bias with increasing the Mn doping. E_b is important in magnetic recording. It is used in fixing the head of hard disk drives with maximum precision. First, E_b is applied to stabilize the ferromagnetic layers in the read heads. Today, change bias fixes the hard reference layer in read head and memory circuits by using magnetic resistance/magnetic tunneling. The E_b material should have magnetocrystalline anisotropy and chemical stability. Table 4 presents the magnetic properties of nanosamples. It can be seen that the M_s, H_c, and

Table 4 Magnetic properties of Cu/Mn co-doped ZnO magnetic NPs

Samples	Coercivity H_c (Oe)	Saturation magnetization M_s (emu/cm^3)	Remnant M_r (emu/cm^3)	Squareness ratio M_r/M_s	Exchange bias $H_{ex} = H_c/2$
Mn1	144.32	0.911	0.112	0.122	72.16
Mn2	106.17	2.418	0.118	0.048	53.08
Mn3	105.41	3.557	0.068	0.019	52.70
Mn4	115.07	4.700	0.141	0.030	57.53
Mn5	162.59	9.216	0.445	0.048	81.29

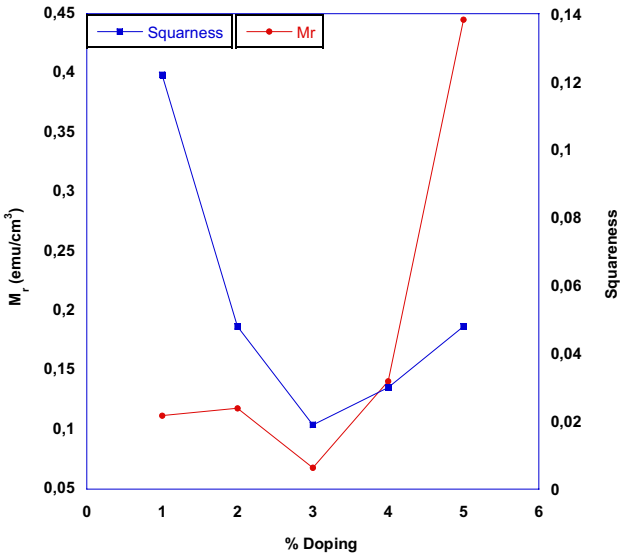

Fig. 9 Remanent magnetization and squareness ratio vs Mn doping

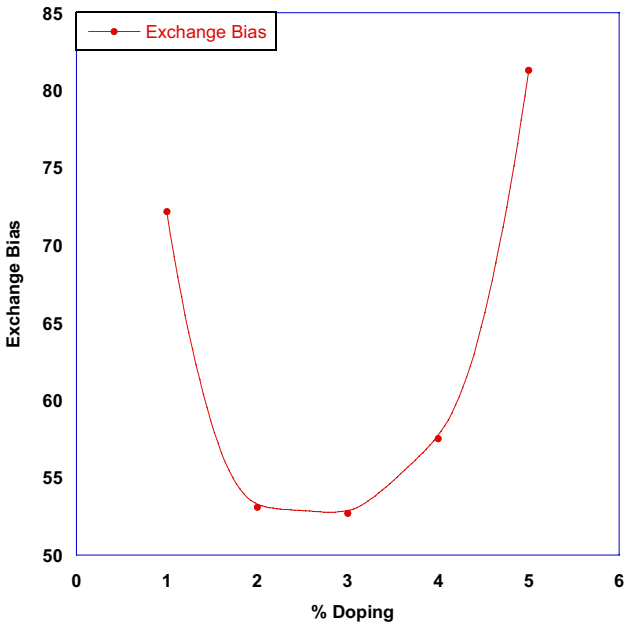

Fig. 10 Change in the exchange bias with an increase in Mn doping

remanence gradually increased with the increase of the Mn doping [42].

The ferromagnetism of thin films originates from the interplay of O vacancies and Mn atoms forming magnetic polarons. The magnetic-exchange interplay between magnetic-defects and polarized spin-carriers causes the formation of bound magnetic polarons (BMP). Mn is paramagnetic [43]. Undoped ZnO has diamagnetic property. The observed ferromagnetism arises from Mn doping, which adapts the magnetic-exchange interplay. Since the carriers are placed by force, the BMP theory can discover the seen magnetism. In the BMP model, the spins of the Mn-doped impurities align with the localized spin. At high Mn contribution rates, the magnetic moments of BMPs are in the same directions and increase the saturation magnetization.

The saturation magnetization of samples is proportional to the size of crystal. Moreover, the Mn contribution rate causes the regular dispersion of BMP without changing the wurtzite lattice. Maximum saturation magnetization at high Mn-doped percentage supports the presence of BMPs in Mn-doped ZnO.

In all DMS thin films, the gap (O or Zn or both) density, exchange mechanism, and secondary phase are responsible for the ferromagnetism. Ferromagnetism at RT can be either extrinsic or intrinsic. X-ray diffraction peaks of samples exhibited only ZnO peaks. Therefore, ferromagnetism is an intrinsic property in Mn-doped ZnO thin films. The replacement of Zn ion with Mn^{+2} ions in the Zinc oxide structure is responsible for the ferromagnetism in thin films. The exchange interplay took place between conducting electrons.

Therefore, because of exchange interplays, the spin of Mn^{+2} ions aligns in parallel with the direction

creating the ferromagnetic properties of the samples. The Mn ions are randomly oriented in the beginning and the oxygen void's coupling creates carriers that randomly generate a magnetic moment. Polarons are created by aligning the magnetic moment in the same direction. The polarons overlap due to oxygen voids and so the ferromagneticity occurs [44, 45].

4 Conclusion

In this study, all $Zn_{1-x}Cu_{0.05}Mn_xO$ QUOTE polycrystalline nanoparticles were produced using various Mn compositions ($0.01 < x < 0.05$) QUOTE with sol–gel techniques. The magnetic and structural properties of Cu/Mn-doped zinc oxide nanoparticles were analyzed at RT.

The crystallinity and structural properties of Cu/Mn co-doped ZnO nanoparticles were examined using XRD analysis in details. XRD peak expansion analysis was conducted in order to calculate the several important parameters of nanocrystals, for example, stress, intrinsic strain, and energy density, whereas W–H, SSP, and H–W methods were used for the determination of the average crystal size. According to these analyses, it was seen that the average size determined from W–H methods was much closer to the Scherrer method. In our case, the UDM, USDM, and UDEDM models are the most suitable models for the evaluation of the average crystal size of ZnO nanoparticles.

Although the $Zn_{1-x}Mn_xO$ system has been extensively studied in recent years, no definite conclusions could be drawn from the experimental results. In the DMS system, it is generally accepted that the source of the magnetism is the interaction between the carriers and the localized magnetic moments associated with the magnetic atoms. Therefore, the concentration of carriers plays an important role in determining the magnetic properties of the system.

The increase of magnetization is related to the increase of oxygen vacancies. To preserve the total load balance, some of O^{-2} ions leave the lattice and cause oxygen gaps. These oxygen gaps bind free charge carriers. The interaction between the charge carriers trapped in the oxygen vacancies and the spin of the Cu ion causes the generation of magnetization by BMPs.

Because of the presence of a large number of oxygen vacancies, the interplay between multiple BMPs causes the formation magnetic field, known as long-distance ferromagnetism. An increase in magnetization together with an increase in Mn doping arises from the preference for parallel spin–spin coupling between Mn ions and close by oxygen ions instead of anti-parallel coupling.

The ferromagnetic coupling between TM ions and bonded polarons can form bonded magnetic polarons that are responsible for the origin of FM in TM–ZnO. Considering the point defects hybridizing with TM doping, defect-based carriers induce RTFM (ferromagnetism at room temperature) in doped ZnO. In $Zn_{0.95-x}Cu_{0.05}Mn_xO$ nanoparticles, a series of O^{-2} gaps (vacancies) are created by doping Mn^{+2} and Cu^{+2} instead of Zn^{+2} and this produces RTFM.

Acknowledgements

This work was supported by Kastamonu University Scientific Research Projects Coordination Department under the Grant No. KÜ-BAP01/2020-75, KÜ-BAP01/2019-64 and Kastamonu University Research and Application Center for the supports.

Author contributions

All authors have contributed sufficiently in the planning, execution, or analysis of this study to be included as authors. All authors have read and agreed to the published version of the manuscript.

Funding

Kastamonu Üniversitesi, KÜ-BAP01/2019–64, O. Ozturk, KÜ-BAP01/2020–75, Elif Asikuzun.

Data availability

The data sharing is not applicable to this article asno datasets were generated or analyzed during the current study.

Declarations

Conflict of interest The authors declare that there is no conflict of interest regarding the publication of this article.

Compliance with Ethical Standards This material is the authors' own original work, which has not been previously published elsewhere. The paper reflects the authors' own research and analysis in a truthful and complete manner. The results are appropriately placed in the context of prior and existing research. All authors have been personally and actively involved in substantial work leading to the paper and will take public responsibility for its content.

References

1. Z.N. Kayani, T. Afzal, S. Riaz, S. Naseem, Optical and structural properties of thin films of ZnO at elevated temperature. J. Alloy. Compd. **606**, 177–181 (2014)
2. Z.N. Kayani, M. Iqbal, S. Riaz, R. Zia, S. Naseem, Fabrication and properties of zinc oxide thin film prepared by sol-gel dip coating method. Mater. Sci. Pol. **33**, 515–520 (2015)
3. Z.N. Kayani, F. Saleemi, I. Batool, Effect of calcination temperature on the properties of ZnO nanoparticles. Appl. Phys. A **119**, 713–720 (2015)
4. K.C. Barick, S. Singh, M. Aslam, D. Bahadur, Porosity and photocatalytic studies of transition metal doped ZnO nanoclusters. Microporous Mesoporous Mater. **134**, 195 (2010)
5. K. Kaviyarasua, C.M. Magdalanec, K. Kanimozhie, J. Kennedya, B. Siddhardhag, E.S. Reddyh, N.K. Rottei, C.S. Sharmai, F.T. Themaa, D. Letsholathebej, G.T. Molak, M. Maaza, Elucidation of photocatalysis, photoluminescence and antibacterial studies of ZnO thin films by spin coating method. J. Photochem. Photobiol. B Biol. **173**, 466–475 (2017)
6. F. Meng, J. Yin, Y.Q. Duan, Z.H. Yuan, L.J. Bie, Co-precipitation synthesis and gas-sensing properties of ZnO hollow sphere with porous shell. Sens. Actuators B **156**, 703 (2011)
7. B. Sathyaseelan, E. Manikandan, K. Sivakumar, J. Kennedy, M. Maaza, Enhanced visible photoluminescent and structural properties of ZnO/KIT-6 nanoporous materials for white light emitting diode (w-LED) application. J. Alloys Compd. **651**, 479–482 (2015)
8. J. Kennedy, P.P. Murmua, J. Leveneura, A. Markwitza, J. Futteraa, Controlling preferred orientation and electrical conductivity of zinc oxide thin films by post growth annealing treatment. Appl. Surf. Sci. **367**, 52–58 (2016)
9. J. Kennedy, A. Markwitz, Z. Li, W. Gao, C. Kendrick, S.M. Durbin, R. Reeves, Modification of electrical conductivity in RF magnetron sputtered ZnO films by low-energy hydrogen ion implantation. Curr. Appl. Phys.. Appl. Phys. **6**, 495–498 (2006)
10. J. Kennedy, P.P. Murmu, J. Leveneur, M.V. Williams, L.R. Moody, T. Maity, V.S. Chong, Enhanced power factor and increased conductivity of aluminum doped zinc oxide thin films for thermoelectric applications. J. Nanosci. Nanotechnol.Nanosci. Nanotechnol. **18**, 1384–1387 (2018)
11. Z. Liu, C. Liu, J. Ya, E. Lei, Controlled synthesis of ZnO and TiO_2 nanotubes by chemical method and their application in dye-sensitized solar cells. Renew. Energy **36**, 1177 (2011)
12. Z. Jin, T. Fukumura, M. Kawasaki, K. Ando, H. Saito, T. Sekiguchi, Y. Yoo, M. Murakami, Y. Matsumoto, T. Hasegawa, High throughput fabrication of transition-metaldoped epitaxial ZnO thin films: A series of oxide-diluted magnetic semiconductors and their properties. Appl. Phys. Lett. **78**, 3824–3826 (2001)
13. F. Pan, C. Song, X. Liu, Y. Yang, F. Zeng, Ferromagnetism and possible application in spintronics of transition-metaldoped ZnO films. Mater. Sci. Eng. R Reports **62**, 1–35 (2008)
14. S. Singh, M.R. Rao, Optical and electrical resistivity studies of isovalent and aliovalent 3 d transition metal ion doped ZnO. Phys. Rev. B **80**, 045210 (2009)
15. S. Singhal, J. Kaur, T. Namgyal, R. Sharma, Cu-doped ZnO nanoparticles: synthesis, structural and electrical properties. Physica B **407**, 1223–1226 (2012)
16. H. Liu, J. Yang, Y. Zhang, L. Yang, M. Wei, X. Ding, Structure and magnetic properties of Fe-doped ZnO prepared by the sol–gel method. J. Phys. Condens. MatterCondens. Matter **21**, 145803 (2009)
17. P.G. Undre, P.B. Kharat, R. Kathare, K. Jadhav, Ferromagnetism in Cu 2+ doped ZnO nanoparticles and their physical properties. J. Mater. Sci. Mater. Electron. **30**, 4014–4025 (2019)
18. D. Raoufi, Synthesis and microstructural properties of ZnO nanoparticles prepared by precipitation method. Renew. Energy **50**, 932 (2013)
19. M.M. Ba-Abbad, A.A.H. Kadhum, A.B. Mohamad, M.S. Takriff, K. Sopian, Optimization of process parameters using D-optimal design for synthesis of ZnO nanoparticles via sol–gel technique. J. Ind. Eng. Chem. **19**, 99 (2013)

20. T. Wangensteen, T. Dhakal, M. Merlak, P. Mukherjee, M.H. Phan, S. Chandra, H. Srikanth, S. Witanachchi, Growth of uniform ZnO nanoparticles by a microwave plasma process. J. Alloys Compd. **509**, 6859 (2011)
21. B. Woeichieng, Y.Y. Loo, Synthesis of ZnO nanoparticles by modified polyol method. Mater. Lett. **73**, 78 (2012)
22. P. Rai, Y.-T. Yu, Citrate-assisted hydrothermal synthesis of single crystalline ZnO nanoparticles for gas sensor application. Sens. Actuators B Chem. **173**, 58 (2012)
23. M. Vaghayenegar, A. Kermanpur, M.H. Abbasi, Bulk synthesis of ZnO nanoparticles by the one-step electromagnetic levitational gas condensation method. Ceram. Int. **38**, 5871 (2012)
24. Y. Liu, Y. Yang, J. Yang, Q. Guan, H. Liu, L. Yang, Y. Zhang, Y. Wang, M. Wei, X. Liu, L. Fei, X. Cheng, Intrinsic ferromagnetic properties in Cr-doped ZnO diluted magnetic semiconductors. J. Solid State Chem. **184**, 1273 (2011)
25. R. Saleh, N.F. Djaja, S.P. Prakoso, The correlation between magnetic and structural properties of nanocrystalline transition metal-doped ZnO particles prepared by the co-precipitation method. J. Alloys Compd. **546**, 48 (2012)
26. F. Ahmed, S. Kumar, N. Arshi, M.S. Anwar, B.H. Koo, C.G. Lee, Doping effects of Co^{2+} ions on structural and magnetic properties of ZnO nanoparticles. Microelectron. Eng.. Eng. **89**, 129 (2012)
27. R. Narzary, B. Dey, S.N. Rout, A. Mondal, G. Bouzerar, M. Kar, S. Ravi, S.K. Srivastava, Influence of K/Mg co-doping in tuning room temperature d0 ferromagnetism, optical and transport properties of ZnO compounds for spintronics applications. J. Alloys Compd. **934**, 167874 (2023)
28. B. Dey, R. Narzary, S.K. Panda, J. Mallick, A. Mondal, S. Ravi, M. Kar, S.K. Srivastava, Room temperature d0 ferromagnetism, band-gap reduction, and high optical transparency in p-type K-doped ZnO compounds for spintronics applications. Mater. Sci. Semicond. Process. Process. **148**, 106798 (2022)
29. B. Dey, R. Narzary, L. Chouhan, S. Bhattacharjee, B.N. Parida, A. Mondal, S. Ravi, S.K. Srivastava, Crystal structure, optical and dielectric properties of Ag:ZnO composite-like compounds. J. Mater. Sci. Mater. Electron. **33**, 2855–2868 (2022)
30. L. Chouhan, G. Bouzerar, S.K. Srivastava, d^0 ferromagnetism in Li-doped ZnO compounds. J. Mater. Sci. Mater. Electron. **32**, 6389–6397 (2021)
31. B. Dey, S. N. Rout, M. Kar, S. K. Srivastava, Room Temperature d^0 Ferromagnetism of Ag:ZnO Compounds, Journal of Superconductivity and Novel Magnetism **36**, 657–663 (2023).
32. V.D. Mote, Y. Purushotham, B.N. Dole, Williamson-Hall analysis in estimation of lattice strain in nanometer-sized ZnO particles. J. Theoret. Appl. Phys. **6**, 6 (2012)
33. E. Emil, S. Gürmen, Estimation of yttrium oxide microstructural parameters using the Williamson-Hall analysis. Mater. Sci. Technol. **34**, 1549–1557 (2018)
34. D. Nath, F. Singh, R. Das, X-ray diffraction analysis by Williamson-Hall, Halder-Wagner and size-strain plot methods of CdSe nanoparticles- a comparative study. Mater. Chem. Phys. **239**, 122021 (2020)
35. S. Sarkar, R. Das, Determination of structural elements of synthesized silver nano-hexagon from X-ray diffraction analysis. Indian J. Pure Appl. Phys. **56**, 765–772 (2018)
36. S. Sarkar, R. Das, Shape effect on the elastic properties of Ag nanocrystals. Micro Nano Lett. **13**, 312–315 (2018)
37. D. Balzar, H. Ledbetter, Voigt-function modeling in fourier analysis of size- and strain-broadened X-ray diffraction peaks. J. Appl. Crystallogr.Crystallogr. **26**, 97–103 (1993)
38. A. Hepp, C. Baerlocher, Learned peak shape functions for powder diffraction data. Aust. J. Phys. **41**, 229–236 (1988)
39. N.C. Halder, C.N.J. Wagner, Separation of particle size and lattice strain in integral breadth measurements. Acta Crystallogr. Crystallogr. **20**, 312–331 (1966)
40. S. Gopinath, JohnPhilip, Preparation of metal oxide nanoparticles of different sizes and morphologies, their characterization using small angle X-ray scattering and study of thermal properties. Mater. Chem. Phys. **145**, 213–221 (2014)
41. A.C. Murrieta, D. Cavazos-Cavazos, P. Santos-Aguilar, J.L. Cholula-Díaz, F.F. Contreras-Torres, Microstructure of polycrystalline gold nanoparticles and thin-films from a comparative X-ray line profile analysis. Mater. Chem. Phys. **258**, 123976 (2021)
42. M. Shobana, S.R. Meher, Structural, optical and magnetic properties of cobalt-doped ZnTe dilute magnetic semiconductors. J. Mater. Sci. Mater. Electron. **31**, 15140–15152 (2020)
43. Z.N. Kayani, A. Usman, H. Nazli, R. Sagheer, S. Riaz, S. Naseem, Dielectric and magnetic properties of dilute magnetic semiconductors Ag-doped ZnO thin films. Appl. Phys. A **126**, 559 (2020)
44. H.B. Wang, H. Wang, C. Zhang, F.J. Yang, J.X. Duan, C.P. Yang, H.S. Gu, M.J. Zhou, Q. Li, Y. Jiang, Preparation and Characterization of Mn and (Mn, Cu) Co-Doped ZnO Nanostructures. J. Nanosci. Nanotechnol.Nanosci. Nanotechnol. **9**, 3308–3312 (2009)
45. A.A. Dakhel, Study of structural, optical and magnetic properties of hydrogenated Ni and (Ga, Zn) co-doped SnO_2 nanocomposites. Mater. Chem. Phys. **252**, 123163 (2020)

Publisher's Note Springer Nature remains neutral with regard to jurisdictional claims in published maps and institutional affiliations.

Springer Nature or its licensor (e.g. a society or other partner) holds exclusive rights to this article under a publishing agreement with the author(s) or other rightsholder(s); author self-archiving of the accepted manuscript version of this article is solely governed by the terms of such publishing agreement and applicable law.